

A central compact object in Kes 79: the hypercritical regime and neutrino expectation

C. G. Bernal^{1★} and N. Fraija^{2★}

¹*Instituto de Matemática, Estatística e Física, Universidade Federal do Rio Grande, Av. Itália km 8 Bairro Carreiros, Rio Grande, 96203-900 RS, Brazil*

²*Instituto de Astronomía, Universidad Nacional Autónoma de México, Circuito Exterior, C.U., A. Postal 70-264, 04510 México D.F., Mexico*

Accepted 2016 July 27. Received 2016 July 19; in original form 2015 November 26

ABSTRACT

We present magnetohydrodynamical simulations of a strong accretion on to magnetized proto-neutron stars for the Kesteven 79 (Kes 79) scenario. The supernova remnant Kes 79, observed with the *Chandra* ACIS-I instrument during approximately 8.3 h, is located in the constellation Aquila at a distance of 7.1 kpc in the galactic plane. It is a galactic and a very young object with an estimate age of 6 kyr. The *Chandra* image has revealed, for the first time, a point-like source at the centre of the remnant. The Kes 79 compact remnant belongs to a special class of objects, the so-called central compact objects (CCOs), which exhibits no evidence for a surrounding pulsar wind nebula. In this work, we show that the submergence of the magnetic field during the hypercritical phase can explain such behaviour for Kes 79 and others CCOs. The simulations of such regime were carried out with the adaptive-mesh-refinement code FLASH in two spatial dimensions, including radiative loss by neutrinos and an adequate equation of state for such regime. From the simulations, we estimate that the number of thermal neutrinos expected on the Hyper-Kamiokande Experiment is 733 ± 364 . In addition, we compute the flavour ratio on Earth for a progenitor model.

Key words: equation of state – magnetic fields – MHD – neutrinos – stars: neutron – supernovae: individual: Kes 79.

1 INTRODUCTION

Central compact objects (CCOs) are point-like sources located at central regions of some supernova remnants (SNRs), which have been observed only in the X-rays (Pavlov, Sanwal & Teter 2004). The X-ray spectra have been characterized to have thermal components with blackbody temperatures of 0.2–0.5 keV and luminosities $L_X \sim 10^{33}–10^{34}$ erg s^{−1}. Several of such sources and their SNRs are well known, including RCW103, Cassiopeia A (Cas A), Pup A and Kes 79 (Kaspi 2010). Currently, it is widely accepted that CCOs are neutron stars born in supernova (SN) explosions with an unusually estimated low magnetic field. A possible explanation for this atypical behaviour is the so-called hidden magnetic field scenario. It suggests that the strong magnetic field has been buried due to a strong accretion during a core-collapse SN (see e.g. Muslimov & Page 1995; Geppert, Page & Zannias 1999; Bernal et al. 2013 and references therein). When the core-collapse SN event takes place, the shock is still pushing its way through the outer layers of the progenitor, and if it encounters a density discontinuity, a reverse shock may be generated. Depending on its strength and how far it was generated, this reverse shock can induce a strong accretion on

to the newborn neutron star on time-scales of hours. Hypercritical accretion results when the accretion rate is higher than Eddington accretion rate ($\dot{M} > \dot{M}_{\text{Edd}}$). In this scenario, photons are trapped within the accretion flow and the energy liberated by the accretion is lost through neutrino emission close to the neutron star surface. After the reverse shock hits the neutron star surface and rebounds, a third shock develops and starts moving outwards against the infalling matter. Once this accretion shock stabilizes, it will separate the infalling matter from an extended envelope in quasi-hydrostatic equilibrium. Based on such scenario of late accretion on to newborn neutron stars inside SNe, Chevalier & Soker (1989) developed an analytical model for the hypercritical regime. In this model, the neutrino cooling plays an important role in the formation of a quasi-hydrostatic envelope around the compact remnant.

In Chevalier (1989), the author highlighted some conditions involved in the formation of neutron stars inside SNe, including the hyperaccretion of material due to reverse shock and the formation of a convective envelope around the compact remnant. Following such ideas, Muslimov & Page (1995) considered the submergence of the magnetic field on the stellar crust and the subsequent ohmic diffusion of the submerged magnetic flux through the outermost nonmagnetic layers of the crust of a newborn neutron star. With these requirements, Geppert et al. (1999) presented simple 1D ideal magnetohydrodynamical (MHD) simulations of the effect of this

* E-mail: cgbernal@furg.br (CGB); nifraija@astro.unam.mx (NF)

post-SN hypercritical accretion on the newborn neutron star magnetic field to show that such submergence/re-emergence could occur. These simulations displayed a rapid submergence of the magnetic field into the neutron star. Based on MHD simulations with high refinement, Bernal, Lee & Page (2010) and Bernal et al. (2013) confirmed this result. After hyperaccretion stops, the magnetic field could diffuse back to the surface, resulting in a delayed switch-on of a pulsar. It is worth noting that depending on the amount of accreted material, the submergence could be so deep that the neutron star may appear and remain unmagnetized for centuries (Geppert et al. 1999). Recently, some authors revisiting this scenario studied the magnetic field evolution in the CCO context (Ho 2011; Viganò & Pons 2012). In addition, Shabaltas & Lai (2012) and Popov, Kaurav & Kaminker (2015) have suggested that such hidden magnetic field scenario may be applicable for various CCOs, including the compact remnant in Kes 79.

Located in the Galactic plane at 33 deg north-east of the Galactic Centre, Kes 79 (also known as G33.6+0.1) is the source 79 in the radio catalogue of Kesteven (Kesteven 1968). It is a moderately large SNR with a point-like source at its centre, widely believed to be a neutron star created in the SN explosion. Such CCO is called CXO J1852.6+0040 (Seward et al. 2003). The authors showed that the luminosity, in the X-ray band (0.3–8 keV), is $\sim 7 \times 10^{33}$ erg s⁻¹, which corresponds to four times the X-ray luminosity reported in the CCO of Cas A. The blackbody spectrum peaking at X-rays and the lack of a pulsar wind nebula indicate that the thermal emission could be originated from a small region, perhaps on the surface of the neutron star. As Popov et al. (2015) pointed out, the hypothesis of their suppressed magnetosphere is mainly based on the analysis of their thermal emission: pulse profiles of the X-ray light curves and a high pulse fraction, which requires magnetar-scale fields in the crust.

Gotthelf, Halpern & Seward (2005) reported the discovery of 105 ms X-ray pulsations from the CCO in Kes 79, with an upper limit on its spin-down rate of $\dot{P} < 7 \times 10^{-14}$ s s⁻¹. Assuming a magnetic dipole model, they estimate that the surface magnetic field strength is $B < 3 \times 10^{12}$ G. Also, if a blackbody model of temperature $T_{\text{BB}} = (0.44 \pm 0.03)$ keV is used for the X-ray spectrum characterization, they estimated a radius for the source of $R_{\text{BB}} \sim 0.9$ km. More recently, Bogdanov (2014) modelled such X-ray pulsations in Kes 79 in the context of thermal surface radiation from a rotating neutron star, and more accurate results for the surface magnetic field were estimated. Taking into account the reasons mentioned above and the similarities between the CCO in Kes 79 and the neutron star in Cas A, in the present work we adopt, for simplicity, standard parameters for the neutron star in Kes 79: $M \simeq 1.44 M_{\odot}$, $R \simeq 10$ km and an average pre-hyperaccretion magnetic field of $B \simeq 10^{12}$ G. Such parameters are adequate for progenitor models of pre-SN in the range 20–40 M_{\odot} as it seems to be the case of Kes 79 (see Chevalier 2005; Shabaltas & Lai 2012 and references therein.) Although we have chosen the Kes 79 CCO as a particular case, the method presented here can be adapted for other CCOs with similar features.

In the hidden magnetic field scenario, the neutrino production and cooling on the neutron star surface play an important role in the formation of a quasi-hydrostatic envelope (Bernal et al. 2013; Fraija, Bernal & Hidalgo-Gaméz 2014; Fraija & Bernal 2015). The properties of these neutrinos get modified when they propagate in this thermal and magnetized medium. For instance, depending on the flavour composition, neutrinos would feel a different effective potential. These changes in the flavour mixing are due to the electron neutrino (ν_e) interaction with electrons via both neutral and charged

currents (CC), whereas muon (ν_{μ}) and tau (ν_{τ}) neutrinos interact only via the neutral current. The resonant conversion of neutrino from one flavour to another caused by the medium effect is well known as the Mikheyev–Smirnov–Wolfenstein effect (Wolfenstein 1978).

Using the FLASH code to simulate the dynamics close to the stellar surface (including the reverse shock, the neutrino-cooling processes and the magnetic field dynamics), some authors presented numerical studies of hypercritical accretion of matter on to the neutron star surface in the centre of the SNRs 1987A and Cas A (Fraija et al. 2014; Fraija & Bernal 2015). The authors estimated the number of neutrinos that must have been seen from the hypercritical accretion episode on the Super-Kamiokande (SK) and Hyper-Kamiokande (HK) neutrino experiments. In this work, we study the dynamics of the envelope and analyse the submergence of the magnetic field into the stellar surface for the compact remnant in Kes 79. We estimate the neutrino flux and the flavour ratio expected on Earth. The paper is arranged as follows. In Section 2, we describe the physics included in the hypercritical model. In Section 3, we show the numerical results from MHD simulations. In Section 4, we study the thermal neutrino dynamics and we analyse the neutrino oscillations. Finally, brief conclusions are drawn in Section 5.

2 PHYSICS INPUT AND NUMERICAL METHOD

Chevalier (2005) showed that progenitors of Type II SN explosions are red supergiants which already have lost their hydrogen envelope via a powerful stellar wind. Then, it is inferred that such progenitors with masses in the range 20–40 M_{\odot} must have a helium core of ~ 6 –7 M_{\odot} and an iron core of ~ 1.5 –1.6 M_{\odot} . In this scenario, a neutron star with $\simeq 1.4 M_{\odot}$ is created. It seems to be the case of Kes 79. As aforementioned, the CCO in Kes 79 looks similar to that CCO present in Cas A (Chakrabarty et al. 2001). If the accretion on to the newly born neutron star surface is hypercritical ($\dot{M} \geq 10^4 \dot{M}_{\text{Edd}}$), where the Eddington accretion rate is $\dot{M}_{\text{Edd}} \sim 10^{18}$ g s⁻¹, then the ram pressure of the falling matter can exceed by several orders of magnitude the superficial magnetic pressure of the neutron star, submerging the magnetic field into the new stellar crust very fast (Bernal et al. 2010, 2013; Fraija et al. 2014). These authors showed that the magnetic field is frozen into the matter and, under certain conditions for the accretion rate and magnetic field, initial configurations of the magnetic field on the neutron star can be rapidly submerged beneath the accreted matter. For instance, Torres-Forné et al. (2016) showed that typical magnetic fields of standard neutron stars can be buried by modest accreted mass of the order of 0.01–0.001 M_{\odot} in the hypercritical phase. This suggests that neutron stars produced by SNe, in which post core-collapse accretion is hypercritical, are born with a weak superficial magnetic field due to the fact that the bulk of the magnetic field was buried into the neutron star crust.

2.1 Structure of the regions

Four dynamically different regions can be identified in the pre-SN: (i) a thin crust formed during the hypercritical phase; (ii) an envelope in quasi-hydrostatic equilibrium; (iii) a free-fall region; and (iv) the external layers of the progenitor. In this context, 1D analytical approaches can be used to estimate some parameters in the system. However, numerical simulations with more degrees of freedom and more physical ingredients are necessary to study in detail the MHD close to the neutron star surface. In Table 1, we

Table 1. Description of the regions during the hypercritical accretion phase.

Zones	Density (g cm ⁻³)	Radii (cm)
I. New crust of NS surface ($r \leq [r_{\text{ns}} + r_c]$)	$\rho_e(r_c/r)^n$	$r_{\text{ns}} = 10^6$; $r_c \sim 200\text{--}400$
II. Quasi-hydrostatic envelope ($[r_{\text{ns}} + r_c] \leq r \leq r_s$)	$7.7 \times 10^2 \left(\frac{r_s}{r}\right)^3$	$r_s \simeq 7.73 \times 10^8$
III. Free-fall ($r_s \leq r \leq r_h$)	$5.74 \times 10^{-2} \left(\frac{r}{r_h}\right)^{-3/2}$	$r_h = 6.3 \times 10^{10}$
IV. External layers ($r_h \leq r \leq r_b$ AND $r > r_b$)	$3.4 \times 10^{-5} \times \begin{cases} \left(\frac{R_*}{r}\right)^{17/7} ; & r_h < r < r_b, \\ \left(\frac{R_*}{r}\right)^{17/7} \frac{(r-R_*)^5}{(r_b-R_*)^5} ; & r > r_b. \end{cases}$	$r_b = 10^{12}$; $R_* \simeq 3 \times 10^{12}$

summarize the densities and radii of each region and also give a brief description as follows.

2.1.1 Zone I: new crust on the stellar surface

When the hypercritical phase takes place, the piled material forms a new crust with a strong magnetic field immersed within it. During this phase, the magnetic field in the range $10^{11} \text{ G} \leq B \leq 10^{13} \text{ G}$ may be submerged and confined into the new crust at $r_{\text{ns}} \leq r \leq (r_{\text{ns}} + r_c)$. Here, $r_{\text{ns}} = 10^6 \text{ cm}$ is the neutron star radius and $r_c \sim 200\text{--}400 \text{ m}$ represents the height-scale of the new crust formed by the accreted matter in the hypercritical phase. Previous simulations performed in Bernal et al. (2010, 2013) showed that this is the case for typical parameters of newly born neutron stars. The density and pressure in the new crust can be modelled as power laws $\rho = \rho_e(r_c/r)^n$ and $p = p_e(r_c/r)^m$, respectively, where ρ_e and p_e are the values at the base of the envelope and n and m are the power indices, which depend on the accretion rate. Radiation and neutrinos confined in this region are thermalized to a few MeV with a neutrino emissivity given by $\dot{\epsilon}_\nu = 0.97 \times 10^{25} (T/\text{MeV})^9 \text{ erg s}^{-1} \text{ cm}^{-3}$ (Dicus 1972). Due to the high dependence of the pair annihilation process with pressure near the stellar surface $p_{e^\pm} = \frac{11}{12} a T^4$, it is possible to write the neutrino emissivity as a function of total pressure (p) as $\dot{\epsilon}_\nu = 1.83 \times 10^{-34} p^{9/4} \text{ erg cm}^{-3} \text{ s}^{-1}$ with a the radiation constant.

2.1.2 Zone II: quasi-hydrostatic envelope

The reverse shock induces hypercritical accretion on to the new-born neutron star surface. The accreted material bounces off the stellar surface forming a new expansive shock, which builds an envelope in quasi-hydrostatic equilibrium around the neutron star, with free-falling material raining over it. The structure of such envelope can be described through density $\rho_{\text{qhe}} = \rho_s \left(\frac{r_s}{r}\right)^3$, pressure $p_{\text{qhe}} = p_s \left(\frac{r_s}{r}\right)^4$ and velocity $v_{\text{qhe}} = v_s \left(\frac{r_s}{r}\right)^{-1}$, where the subscript s refers to the value of density (ρ_s), pressure (p_s) and velocity (v_s) at the shock front and the shock radius $r_s \simeq 7.73 \times 10^8 \text{ cm}$ (Chevalier & Soker 1989). The pressure p_s and density ρ_s are determined by the strong shock condition $p_s = \frac{6}{7} \rho_0 v_0^2$ and $\rho_s = 7 \rho_0$, respectively and v_s by the mass conservation $v_s = -\frac{1}{7} v_0$. Here ρ_0 and v_0 are the density and velocity just outside the shock, respectively. It is worth noting that the quasi-hydrostatic envelope solution described here corresponds to a $\gamma = 4/3$ polytrope. Using the analytical

formula for the neutrino emissivity (Dicus 1972), the radial location of the accretion shock that is controlled by the energy balance between the accretion power and the integrated neutrino losses is $GM\dot{M}/R = \pi R^3 \dot{\epsilon}_\nu$. Then, the high pressure near the neutron star surface which is given by $p_{\text{ns}} \simeq 1.86 \times 10^{-12} \text{ dyn cm}^{-2} \dot{M} r_s^{3/2}$ allows the pair neutrino process to be the dominant mechanism in the neutrino cooling. From the strong shock conditions, we get $\rho_{\text{qhe}}(r) = 7.7 \times 10^2 \left(\frac{r_s}{r}\right)^3 \text{ g cm}^{-3}$, where the quasi-hydrostatic envelope radius lies in the range $(r_{\text{ns}} + r_c) \leq r \leq r_s$.

2.1.3 Zone III: the free-fall region

In the free-fall region, material starts falling with the velocity $v_{\text{ff}}(r) = \sqrt{\frac{2GM}{r}}$ and density profiles $\rho_{\text{ff}}(r) = \frac{\dot{M}}{4\pi r^2 v(r)}$. Requiring the typical values for such object, $M \sim 1.4 M_\odot$ and $\dot{M} \sim 10^3 M_\odot \text{ yr}^{-1}$, the velocity is $v_{\text{ff}}(r) = 7.81 \times 10^7 (r/r_h)^{-1/2} \text{ cm s}^{-1}$ and the density of material in free-fall is $\rho_{\text{ff}}(r) = 5.74 \times 10^{-2} (r/r_h)^{-3/2} \text{ g cm}^{-3}$, where $r_s \leq r \leq r_h$ with $r_h = 6.3 \times 10^{10} \text{ cm}$.

2.1.4 Zone IV: the external layers

By considering a typical profile for a pre-SN, the density of the external layers can be described as $\rho_0 \left(\frac{R_*}{r}\right)^{17/7}$ for $r_h < r < r_b$ and $\rho_0 \left(\frac{R_*}{r}\right)^{17/7} \frac{(r-R_*)^5}{(r_b-R_*)^5}$ for $r > r_b$ with $\rho_0 = 3.4 \times 10^{-5} \text{ g cm}^{-3}$, $r_b = 10^{12} \text{ cm}$ and $R_* \simeq 3 \times 10^{12} \text{ cm}$ (Chevalier & Soker 1989).

2.2 Numerical method

To tackle numerically the hypercritical accretion problem, we use a customized version of the Eulerian numerical code FLASH (Fryxell et al. 2000). We use the Split Eight-Wave solver to solve the whole set of MHD equations. The eight-wave MHD solver is based on a finite-volume, cell-centred method that was proposed by Powell et al. (1999). The solver uses directional splitting to evolve the MHD equations. It makes one sweep in each spatial direction to advance physical variables from one time level to the next. In each sweep, the unit uses adaptive-mesh-refinement (AMR) functionality to fill in guard cells and impose boundary conditions. Then, it reconstructs characteristic variables and uses these variables to compute time-averaged interface fluxes of conserved quantities. In order to enforce conservation at jumps in refinement, the solver makes flux conservation calls to AMR, which redistributes affected fluxes using the

appropriate geometric area factors. Finally, the solver updates the solution and calls the equation of state (EOS) unit to ensure thermodynamical consistency. A difficulty particularly associated with solving the MHD equations numerically lies in the solenoidality of the magnetic field. The notorious $\nabla \cdot \mathbf{B} = 0$ condition, a strict physical law, is very hard to satisfy in discrete computations. Being only an initial condition of the MHD equations, it enters the equations indirectly and is not, therefore, guaranteed to be generally satisfied unless special algorithmic provisions are made. FLASH provides the truncation-error cleaning method for the eight-wave MHD unit as was described in Powell et al. (1999). We work in the ideal MHD regime with only numerical resistivity and viscosity. This is justified due to the violence and short duration of the hypercritical phase. FLASH code solves the equations of compressible ideal and non-ideal MHD in one, two and three dimensions on a Cartesian system. The code is suitable for simulations of ideal plasmas in which magnetic fields can be so strong (or weak) that they do not cause temperature anisotropies (i.e. physically consistent). In principle, they can have any initial configuration.

Here, we are interested in analysing the formation of the envelope around the neutron star and the subsequent building of the new crust (with the magnetic field confined inside), from the initial reverse shock in free-fall until the establishment of the atmosphere in quasi-hydrostatic equilibrium. The external layers are not dynamically important in this part of the work, and therefore not considered in the simulations.

2.2.1 Equation of state

The thermal pressure is a scalar quantity and as given in regular hydrodynamics, it is obtained from the internal energy and density using the equation of state. The matter equation of state is an adaptation of FLASH's Helmholtz package which includes contributions from the nuclei, e^\pm pairs, radiation and the Coulomb correction. This routine is appropriate for addressing astrophysical phenomena in which electrons and positrons may be relativistic and/or degenerate, and radiation may significantly contribute to the thermodynamic state. The Helmholtz Unit in FLASH provides a table of the Helmholtz free energy (hence the name) and makes use of a thermodynamically consistent interpolation scheme obviating the need to perform the complex calculations required of the intrinsic formalism during the course of a simulation. The interpolation scheme uses a biquintic Hermite interpolant resulting in an accurate EOS that performs reasonably well. A detail description of the Helmholtz equation of state is provided by Timmes & Swesty (2000). The range of validity of the Helmholtz Unit in the FLASH code is

$$10^{-10} < \rho < 10^{10} \text{ g cm}^{-3} \quad \text{and} \quad 10^4 < T < 10^{10} \text{ K}. \quad (1)$$

As in our analysis we exceed this range, we make an extension to the equation of state for degenerate regime ($\rho, T > 10^{10}$ units).

2.2.1.1 Ions.

In this case (degenerated regime), we propose a simple analytical relation for the specific energy, pressure and entropy ($\epsilon_{\text{dg}}^{\text{ions}}, P_{\text{dg}}^{\text{ions}}, S_{\text{dg}}^{\text{ions}}$) and their gradients, which fits successfully the numerical results of equations of state for degenerate matter as indicated in Timmes & Swesty (2000):

$$\epsilon_{\text{dg}}^{\text{ions}} = k\rho \rightarrow \frac{d\epsilon}{d\rho} = k, \quad \frac{d\epsilon}{dT} = 0, \quad (2)$$

$$P_{\text{dg}}^{\text{ions}} = k\rho^2 \rightarrow \frac{dP}{d\rho} = 2k\rho, \quad \frac{dP}{dT} = 0, \quad (3)$$

$$S_{\text{dg}}^{\text{ions}} = 0 \rightarrow \frac{dS}{d\rho} = 0, \quad \frac{dS}{dT} = 0, \quad (4)$$

where $k = 2.7941 \times 10^4$ is a proportionality constant calculated in the transitional regime and the subindex dg refers to degeneracy.

2.2.1.2 *Electron-positron pairs* (e^\pm). The total specific electron energy and its gradients are calculated through the degenerated and pair contributions, which are given by

$$\epsilon_{\text{elec}} = \sqrt{\epsilon_{\text{dg}}^2 + \epsilon_{\text{par}}^2}, \quad (5)$$

and

$$\frac{d\epsilon_{\text{elec}}}{d\rho} = \frac{\epsilon_{\text{dg}} \frac{d\epsilon_{\text{dg}}}{d\rho} + \epsilon_{\text{par}} \frac{d\epsilon_{\text{par}}}{d\rho}}{\epsilon_{\text{elec}}}, \quad (6)$$

$$\frac{d\epsilon_{\text{elec}}}{dT} = \frac{\epsilon_{\text{dg}} \frac{d\epsilon_{\text{dg}}}{dT} + \epsilon_{\text{par}} \frac{d\epsilon_{\text{par}}}{dT}}{\epsilon_{\text{elec}}}, \quad (7)$$

where the contribution of degeneracy is given by $\epsilon_{\text{dg}} = \frac{3}{4} \frac{n_e}{\rho} E_F [1 + \frac{2}{3} \pi^2 (k_B T / E_F)^2] = A \rho^{1/3} (1 + B \rho^{-2/3} T^2)$, where A and B are given by $A = \frac{3Y_e^{4/3} (3\pi^2)^{1/3}}{4m_H^{4/3}}$, $B = \frac{3\pi k_B m_H^{1/3}}{(24\pi^2 Y_e)^{1/3}}$, $n_e = Y_e \rho / m_H$ is the electronic density, m_H being the hydrogen mass, $Y_e = Z/A$ is the electronic fraction and $E_F = (3\pi^2)^{1/3} n_e^{1/3}$ is the Fermi energy. The contribution of pairs is $\epsilon_{\text{par}} = \frac{7}{4} \epsilon_{\text{rad}} = \frac{7}{4} \frac{aT^4}{\rho}$. Taking into account the previous relations, the gradients of the high degeneration contribution for the specific energy can be written as

$$\frac{d\epsilon_{\text{dg}}}{d\rho} = \frac{1}{3} A \rho^{-2/3} (1 - B \rho^{-2/3} T^2), \quad (8)$$

$$\frac{d\epsilon_{\text{dg}}}{dT} = 2AB \rho^{-1/3} T, \quad (9)$$

and the pair contribution is

$$\frac{d\epsilon_{\text{par}}}{d\rho} = -\frac{7}{4} \frac{aT^4}{\rho^2} = -\frac{\epsilon_{\text{par}}}{\rho}, \quad (10)$$

$$\frac{d\epsilon_{\text{par}}}{dT} = 7 \frac{aT^3}{\rho} = \frac{4}{T} \epsilon_{\text{par}}. \quad (11)$$

On the other hand, the pressure and its gradient associated are given by

$$P_{\text{dg}} = \frac{1}{3} \rho \epsilon_{\text{elec}}, \quad (12)$$

$$\frac{dP}{dT} = \frac{1}{3} \rho \frac{d\epsilon_{\text{elec}}}{dT}, \quad \frac{dP}{d\rho} = \frac{1}{3} \epsilon_{\text{elec}}. \quad (13)$$

Finally, the total entropy is

$$S_{\text{T}} = \sqrt{S_{\text{dg}}^2 + S_{\text{par}}^2}, \quad (14)$$

and their gradients can be written as

$$\frac{dS_{\text{T}}}{d\rho} = \frac{S_{\text{dg}} \frac{dS_{\text{dg}}}{d\rho} + S_{\text{par}} \frac{dS_{\text{par}}}{d\rho}}{S_{\text{T}}}, \quad (15)$$

$$\frac{dS_{\text{T}}}{dT} = \frac{S_{\text{dg}} \frac{dS_{\text{dg}}}{dT} + S_{\text{par}} \frac{dS_{\text{par}}}{dT}}{S_{\text{T}}}, \quad (16)$$

where the entropy of the degeneracy is $S_{\text{dg}} = \int_0^T \frac{C_V}{T} dT = 2AB \rho^{-1/3} T = \frac{d\epsilon_{\text{dg}}}{dT}$ with the heat capacity at constant volume $C_V = \frac{d\epsilon_{\text{dg}}}{dT} = 2AB \rho^{-1/3} T$ and the contribution of pairs to the entropy is $S_{\text{par}} = \frac{7}{4T} \left[\frac{P_{\text{rad}}}{\rho} + \epsilon_{\text{rad}} \right] = \frac{7}{3} \left[\frac{aT^3}{\rho} \right]$. The gradients to the

case of degeneracy and pairs are

$$\frac{dS_{\text{dg}}}{d\rho} = -\frac{2}{3}AB\rho^{-\frac{4}{3}}T = -\frac{S_{\text{dg}}}{3\rho}, \quad (17)$$

$$\frac{dS_{\text{dg}}}{dT} = 2AB\rho^{-\frac{1}{3}} = \frac{1}{T}S_{\text{dg}} \quad (18)$$

$$\frac{dS_{\text{par}}}{d\rho} = \frac{7}{4}\frac{dS_{\text{rad}}}{d\rho} = -\frac{S_{\text{par}}}{\rho}, \quad (19)$$

$$\frac{dS_{\text{par}}}{dT} = 7\frac{aT^2}{\rho} = \frac{3}{T}S_{\text{par}}. \quad (20)$$

Implementing these corrections in the Helmholtz Unit of the FLASH code, we take into account the contributions of degenerate and relativistic particles for the equation of state, with the conditions $\rho > 10^{10} \text{ g cm}^{-3}$ and $T > 10^{10} \text{ K}$.

2.2.2 Neutrino-cooling processes

Simulations of the neutrino emission and their interactions have found that they carry out a leading role in the dynamics of supernovae and the recently born neutron star so-called proto neutron star (PNS) (see Scholberg 2012; Rrapaj et al. 2015 and references therein). In the hypercritical accretion phase, the neutrino energy losses are dominated by the annihilation process ($e^+ - e^- \rightarrow \nu + \bar{\nu}$), which involves the formation of a neutrino–antineutrino pair. In the present work, we include additionally other relevant neutrino processes present in such regime: (i) the photo-neutrino process. This process is described by the outgoing photon in a Compton scattering going to a neutrino–antineutrino pair ($\gamma + e^\pm \rightarrow e^\pm + \nu + \bar{\nu}$); (ii) the plasmon decay process. It occurs when a photon propagating within an electron gas (plasmon) is spontaneously transformed in a neutrino–antineutrino pair ($\gamma \rightarrow \nu + \bar{\nu}$); and (iii) the bremsstrahlung process. It takes place when a photon is replaced by a neutrino–antineutrino pair, either due to electron–nucleon interactions ($e^\pm + N \rightarrow e^\pm + N + \nu + \bar{\nu}$) or nucleon–nucleon interactions ($N + N \rightarrow N + N + \nu + \bar{\nu}$). All these processes have been well described by Itoh et al. (1996). In their work, the authors have summarized the results of the calculations of the neutrino energy-loss rates resulting from pair, photo-, plasma, bremsstrahlung and recombination neutrino processes based on the Weinberg–Salam theory (Bilenky & Hošek 1982). A wide density–temperature regime $1 \leq \rho/\mu_e \leq 10^{14} \text{ g cm}^{-3}$ and $10^7 \leq T \leq 10^{11} \text{ K}$ has been considered. In the present work, we use the extensive numerical tables for the neutrino processes above mentioned as FORTRAN routines, including the interpolation formulae of the tables and the analytic fitting formulae, implemented in a customized module in FLASH. We consider initially radial profiles for the pressure and density, implying a radial distribution for the energy. However, in the neutrosphere (i.e. the region where neutrinos are produced), we have assumed that mean neutrino energy is around $k_B T$ and all emitted neutrinos have this energy. The numerical routine applies the neutrino-cooling source term operator to a block of zones. The neutrino loss rate is used to update the internal energy in the zone. After we call neutrino-cooling routine, call the EOS to update the pressure and temperature based on the neutrino losses. This implementation in FLASH prevents stiffness problems that may arise in the simulation. Moreover, the main sources of neutrino opacity are then coherent scattering of neutrons and protons, and pair annihilation.

For example, the corresponding cross-section for coherent scattering is $\sigma_N = (1/4)\sigma_0[E_\nu/(m_e c^2)]^2$, where $\sigma_0 = 1.76 \times 10^{-44} \text{ cm}^2$. As neutrinos are created in a thermal medium with temperatures $T \lesssim 10^{11} \text{ K} \lesssim 8 \text{ MeV}$, their energies can be estimated by $E_\nu \sim k_B T$ and the cross-section would be $\sigma_N \lesssim 7 \times 10^{-42} \text{ cm}^2$. The maximum densities reached at the bottom of the envelope become $\rho \sim 10^{10} \text{ g cm}^{-3}$, and in such conditions, the neutrino mean free-path would be $l_\nu = (n_N \sigma_N)^{-1} \gtrsim 2.5 \times 10^6 \text{ cm}$, which is safely larger than the depth of the dense envelope (of order of a few km). Above this dense region, the envelope density decreases rapidly and the whole envelope is practically transparent to neutrinos. We will, hence, ignore neutrino absorption and heating. As in previous works, no nuclear reactions are taken into account.

2.2.3 Initial and boundary conditions

As explained in Bernal et al. (2013), we want to simulate a portion of the surface of the neutron star (spherical geometry) doing a mapping of the surrounding cone above the neutron star into an accreting column (Cartesian geometry). Due to the MHD equations, it can be successfully solved by FLASH in Cartesian coordinates and also the computational cost is minor. This implies that all variables and parameters of the physical model are mapped from a spherical to a Cartesian geometry, without loss of generality. For our two-dimensional computational domain, we consider wide columns with a base of $\Delta x = 2 \times 10^6 \text{ cm}$ (centred on $x = 0$), and a height Δy of $40 \times 10^6 \text{ cm}$, with $y = 10^6 \text{ cm}$ being the neutron star radius. We chose this height-scale to prevent the shock from leaving the computational domain during the initial transient. The gravitational acceleration (plane-parallel external field) is taken as $g_y = -GM/y^2$, and a standard neutron star mass of $1.44 M_\odot$ is assumed.

As magnetic initial condition, we consider a magnetic field loop, in the shape of a hemi-torus. The reason is that, as showed in Bernal et al. (2010, 2013), under certain conditions of accretion rate, any initial magnetic field configuration will be submerged in the hypercritical regime by the accreted matter. However, a magnetic loop is very interesting because the magnetic tension due to the magnetic field curvature can play an important role in the plasma dynamics very close to the stellar surface. On the central hemi-circle of the loop, the field has a strength $B_0 = 10^{12} \text{ G}$ (standard for neutron stars) and it is shaped as a Gaussian, i.e. with strength

$$B(d) = B_0 \times \exp\left(-\frac{d}{R_L}\right)^2, \quad (21)$$

where d is the distance to the loop central hemi-circle and the thickness of the loop is $R_L = 1 \text{ km}$. The two feet of the loop are centred at $x = -5$ and $+5 \text{ km}$. As boundary conditions, we impose mass inflow along the top edge of the computational domain with constant hypercritical accretion rate, and periodic conditions along the sides, allowing fluid to move freely through it. At the bottom, on the neutron star surface, we use a custom boundary condition which enforces hydrostatic equilibrium. In order to establish this boundary, we fix the velocities as null in all the guard cells ($v_x = v_y = 0$), and copy the density and the pressure of the first zone of the numerical domain. This zone corresponds to the neutron star surface ($\rho = \rho(ic)$, $p = p(ic) + \rho v^2 + \rho g y$), where ic is the first zone in the domain, ρv^2 represents the ram pressure and $\rho g y$ is the vertical pressure at

the guard cells. The other thermodynamic variables are calculated from the equation of state. For the magnetic field, the two lateral sides are also treated as periodic boundaries, while at the bottom the field is frozen from the initial condition, i.e. the two feet of the loop are anchored into the neutron star and no field can be pushed into the star by the accretion. On the top boundary, the magnetic field is set to zero, i.e. we assume the accreting matter to be non-magnetized.

On the other hand, our initialization sets the matter in free-fall on to the magnetic loop and we allow the code to find the correct radial profiles of density, pressure, velocity and magnetic field, once the system has been relaxed. Also, we can find a relationship between the shock radius in the Cartesian accretion column projection, y_{sh} , and the accretion rate from analytical considerations. Neutrino losses are dominated mainly by e^\pm pair annihilation for which a simple rate is given by Dicus (1972) as $\dot{\epsilon}_v \simeq 0.97 \times 10^{25} (T/\text{MeV})^9 \text{ erg s}^{-1} \text{ cm}^{-3}$. For given \dot{M} and R , and a fixed \dot{M} , the vertical location of the accretion shock is controlled by energy balance between the accretion power and the integrated neutrino losses, per unit neutron star surface area,

$$\frac{GM\dot{M}}{R} = \int_R^\infty \dot{\epsilon}_v(y) dy. \quad (22)$$

Due to the resulting strong y dependence of $\dot{\epsilon}_v$, the value of the upper limit in the integral of equation (22) is not very important and it fixes the height of the accretion shock in the Cartesian column as

$$y_{\text{sh}} \simeq 5.1 \times 10^6 (\dot{M}_0/\dot{M})^{10/63} \text{ cm} \simeq 4.2 \times 10^6 \text{ cm}, \quad (23)$$

where $\dot{M}_0 \sim 340 M_\odot \text{ yr}^{-1}$ is a fiducial accretion rate estimated for SN 1987A. The hypercritical accretion rate \dot{M} , for the present case, can be estimated following Chevalier (1989) which is written as

$$\dot{M} \simeq 1.2 \times 10^{-4} \left(\frac{t_0}{10 \text{ d}} \right)^{-\frac{1}{3}} \left(\frac{t}{\text{yr}} \right)^{-\frac{5}{3}} M_\odot \text{ yr}^{-1}. \quad (24)$$

It was obtained considering the fact that because of the increasing transparency of the expanding gas, the flow eventually becomes ballistic and the accretion rate is expected to drop as $t^{-5/3}$. As was pointed by Woosley, Langer & Weaver (1993), the late accretion rate depends on the time t_0 , at which this transition is made and for the parameters of a compact remnant like the Kes 79 case, it can be estimated as ~ 5 –10 d. It is estimated that the hypercritical phase takes of the order of hours.

In our simulations, we use the AMR capabilities of the FLASH code with six levels of refinement, which implies an effective resolution of 512×10240 zones in the computational domain. The time step in the FLASH code is adaptive and depends on local conditions. Typically, the time resolution of the simulations is $dt = 10^{-6}$ s.

3 NUMERICAL RESULTS

Our simulations ran for various hundred milliseconds. We found that for the estimated hyperaccretion rate for the Kes 79 scenario, the magnetic field is submerged into the new crust very fast. Neglecting convection effects, the time-scale required for the quasi-stationary solution to set in is a few sound crossing times, $t_{\text{cross}} \simeq r_{\text{shock}}/c_s$. For a shock radius of $\simeq 50$ km and $c_s \simeq c/10$, it is $t_{\text{cross}} \simeq 1$ –2 ms. The simulations presented here run for almost hundreds of ms, so this is established quite fast. The time-scale for convection is of course much longer, and will depend on the equilibrium between infall and cooling at the base of the envelope. In Fig. 1, we show colour maps of pressure, density (on a logarithmic scale) and the magnetic field

(on a linear scale), for the Kes 79 scenario, when quasi-hydrostatic envelope has been established ($t \simeq 150$ ms). We found that in the density and pressure contrast the piling up of accreted matter close to the neutron star surface is very notorious (an effect not accounted for in the analytical approach). In addition, although the system has reached a quasi-stationary state, little turbulent motion remains in the system, just above the neutron star surface, which is clearer in the magnetic field contrast. It can be explained due to the presence of the confined strong magnetic field, and because of the periodic boundary condition on the vertical sides, matter can freely flow in the horizontal direction, as well as bounce off the neutron star surface, which prevents a full stationary state from being reached. In our simulations, we obtain a value of $y_{\text{sh}} \simeq 4.0 \times 10^6$ cm, in agreement with the analytical approach. It is worth noting that a stationary envelope, in quasi-hydrostatic equilibrium, will expand, or shrink, so that the physical conditions at its base allow neutrinos to carry away all the energy injected by the accretion. Once emitted, neutrinos will act as an energy sink provided the material is optically thin to them. It causes an imbalance in pressure at the base of the column accretion. This fact allows the piling up of matter on to the neutron star surface building a new crust with the bulk of the magnetic field buried by the hyperaccretion in the same height-scale. For the present scenario, the high density due to the strong accretion submerges the magnetic field into the crust deep, quickly and efficiently. In Fig. 2, we show colour maps of ram pressure (on a logarithmic scale) and the ratios of ram pressure to magnetic pressure and magnetic pressure to thermal pressure (on a linear scale) for a comparative analysis. Here, the ram pressure is defined as $p_{\text{ram}} = \rho v^2$ and the magnetic pressure is, basically, $p_B = B^2/8\pi$. The thermal pressure is obtained directly from the equation of state. In the ram-pressure panel, we show the quasi-hydrostatic envelope well established with the infalling matter raining over it. We note that the flow smooths gradually as the accretion shock stabilizes. Instabilities of the Rayleigh–Taylor type are present in this regime, but they disappear when the system reaches equilibrium. The initial magnetic loop configuration was immediately torn apart by the reverse shock and the initial strong convection which is dragging the field with it within the developing envelope ($t = 1$ ms). As expected, the ram pressure is dominant inside the envelope, mainly near the stellar surface. The free-fall region has a ram pressure two orders of magnitude lower. The magnetic-pressure to ram-pressure panel is confirming the dominance of the ram pressure on the magnetic pressure in most of the computational domain, except in the region where the magnetic field remains confined, because there these pressures are comparable. Nevertheless, as the matter continues to fall during the whole hypercritical phase, the ram pressure eventually overtakes the magnetic pressure, submerging the bulk of the magnetic field in the new crust formed with the accreted matter. In Bernal et al. (2013), the authors performed numerical simulations with similar and larger accretion rates and found that the magnetic field submergence is more notorious and efficient for larger accretion rates. To compare the magnetic pressure $p_B = B^2/8\pi \sim 10^{23} (B/10^{12} \text{ G})^2$ to the thermal pressure p , when the envelope in quasi-hydrostatic equilibrium has been established, we can use its previous definitions to deduce

$$p = 3.26 \times 10^{28} (\dot{M}/\dot{M}_0)^{4/9} (10 \text{ km/y})^4 \text{ dyn cm}^{-2}. \quad (25)$$

It is worth noting that the Kes 79 hyperaccretion rate is always in the regime $p_B \ll p$. This result has been confirmed by comparing the magnetic-pressure to thermal-pressure panel. Although in the first stages, the system has a turbulent dynamics, the magnetic field, having its feet frozen into the neutron star surface, always remains

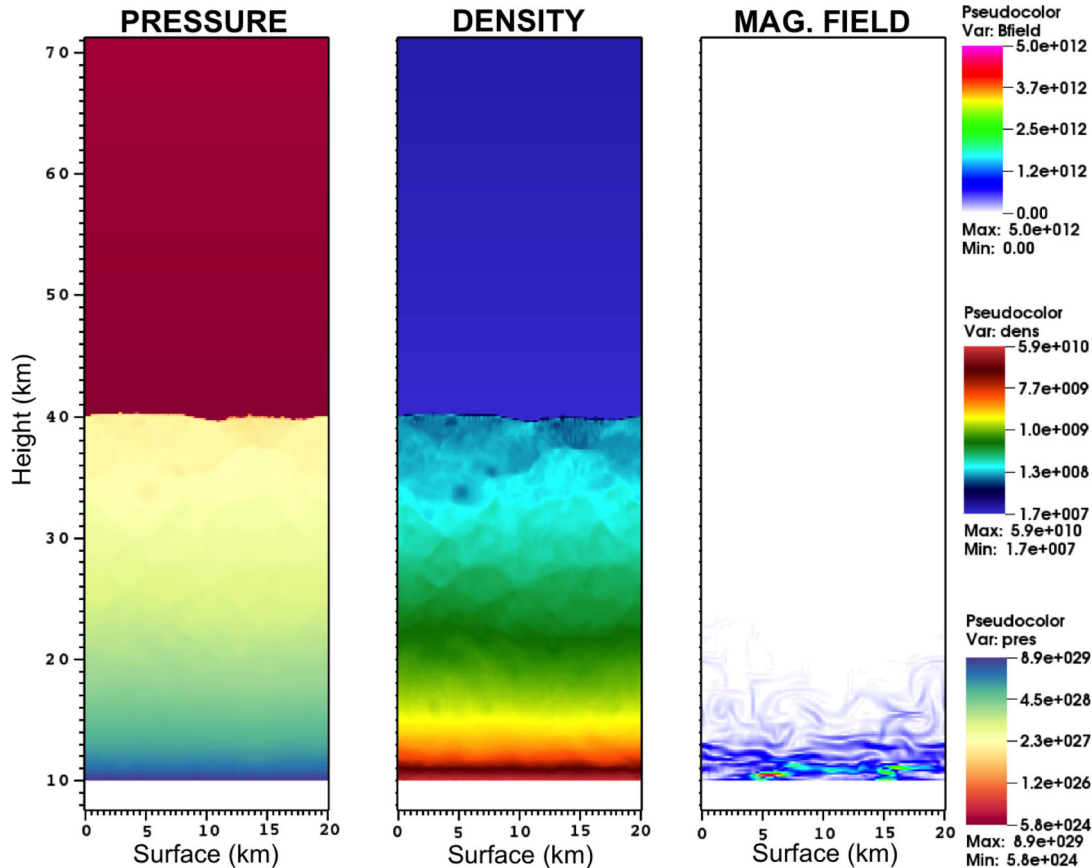


Figure 1. Colour maps of pressure and density (on a logarithmic scale), as well as the magnetic field magnitude (on a linear scale) for the Kes 79 hyperaccretion rate. We show 2D MHD simulations, when a quasi-hydrostatic envelope has been established ($t = 150$ ms). Note the formation of the new crust and the submergence of the magnetic field in the same height-scale.

confined below the accretion shock. After 40 ms, the magnetic field begins to be submerged and is trapped into the material that is piling up on to the neutron star surface. The matter outside the accretion shock is still falling with constant accretion rate, but it is the fluid inside the envelope, with its much lower downward velocity, which is nevertheless responsible for the magnetic field submergence. After 150 ms, the submergence is completed, with a maximum strength of the magnetic field $\simeq 6 \times 10^{12}$ G.

In Fig. 3, we show the radial profiles of density, pressure and temperature (on a logarithmic scale), as well as the magnetic field magnitude (on a linear scale), when the quasi-hydrostatic envelope has been established. In the density and pressure profiles, the piling up of matter close to the neutron star surface is very notorious, but in the temperature profile this behaviour is less notorious. In addition, the magnetic field has been amplified since its seminal value by a factor of 6. This may be due to a turbulent dynamo mechanism acting on the crust. However, this hypothesis requires further study that is beyond the scope of this paper. Of course, the question of how the flow approaches the steady state in a time-dependent situation remains an open problem. However, numerical simulations with more refinement, more physical ingredients and more degrees of freedom in the system offer new and unique insight into this problem. As noted by Bernal et al. (2010), the study of quasi-hydrostatic envelopes around neutron stars poses a challenge. It is a runaway process in which the neutrino losses lead to the gravitational contraction of the envelope, increasing the

pressure at the base of the envelope, which increases the neutrino losses.

The neutrino emission is strongly concentrated within the first kilometre above the stellar surface due to the strong temperature dependence of the emissivity. In Fig. 4, we show a colour map of the neutrino emissivity, in linear scale, when the quasi-stationary state is reached. The mean emissivity in such region is $\dot{\epsilon}_\nu \simeq 2 \times 10^{31}$ erg s $^{-1}$ cm $^{-3}$ and the mean neutrino luminosity is then $L_\nu = \dot{\epsilon}_\nu \times V \simeq 8 \times 10^{48}$ erg s $^{-1}$, with the volume of the region $V = (2 \times 10^6)^2 \times (10^5) = 4 \times 10^{17}$ cm 3 .

4 NEUTRINOS

4.1 Events expected in the HK Experiment

The HK observatory will be the third generation of water Cherenkov detector in Kamioka, designed for a vast variety of neutrino studies. At a distance of 8 km from its predecessor SK, the HK detector will be built as the Tochibora mine of the Kamioka Mining and Smelting Company, near Kamioka town in the Gifu Prefecture, Japan. It will be composed of two separate caverns, each having an egg-shaped cross-section of 48 m wide, 54 m tall and 250 m long. The entire array will be made up of 99,000 photomultiplier tubes, uniformly surrounding the region. It will have a total (fiducial) mass of 0.99 (0.56) million metric tons, approximately 20 (25) times larger than that of SK. Among the physical potentials of this detector, SK

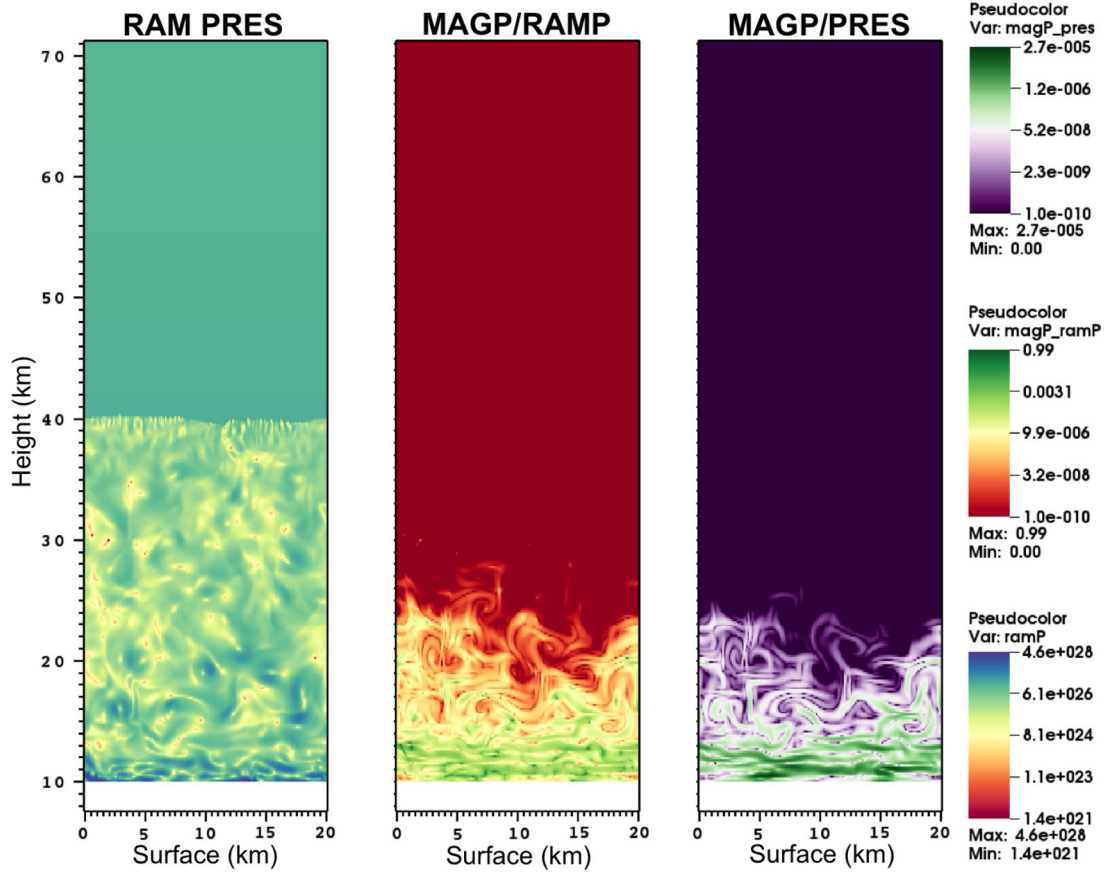


Figure 2. Colour maps of ram pressure, ratios of magnetic pressure to ram pressure and magnetic pressure to thermal pressure, for the Kes 79 hyperaccretion rate for a comparative analysis, in $t = 150$ ms. Note the dominance of the ram pressure over the magnetic pressure allowing the magnetic field submergence.

will be focused on the detection of astrophysical neutrinos and the studies of neutrino oscillation parameters (Abe et al. 2011; Hyper-Kamiokande Working Group et al. 2014).

It is possible to estimate the numbers of events to be expected in this observatory. The number of events to be expected can be written as (Fraija & Araya 2016)

$$N_{\text{ev}} = t V N_A \rho_N \int_{E'} \sigma_{\text{cc}}^{\bar{\nu}_e p} \frac{dN}{dE} dE, \quad (26)$$

where V is the effective water volume, $N_A = 6.022 \times 10^{23} \text{ g}^{-1}$ is the Avogadro number, $\rho_N = 2/18 \text{ g cm}^{-3}$ is the nucleon density, $\sigma_{\text{cc}}^{\bar{\nu}_e p} \simeq 9 \times 10^{-44} E_{\bar{\nu}_e}^2 / \text{MeV}^2$ is the cross-section, t is the observed time (Fraija & Marinelli 2015) and dN/dE is the neutrino spectrum. Regarding the relationship between the neutrino luminosity L and flux F , $L = 4\pi d_z^2 F \langle E \rangle = 4\pi d_z^2 E^2 dN/dE$ (Fraija 2014a,b) and approximation of the time-integrated average energy $\langle E_{\bar{\nu}_e} \rangle$ and time, then this number is

$$\begin{aligned} N_{\text{ev}} &\simeq \frac{t}{\langle E_{\bar{\nu}_e} \rangle} V N_A \rho_N \sigma_{\text{cc}}^{\bar{\nu}_e p} \langle E_{\bar{\nu}_e} \rangle^2 \frac{dN}{dE} \\ &\simeq \frac{t}{4\pi d_z^2 \langle E_{\bar{\nu}_e} \rangle} V N_A \rho_N \sigma_{\text{cc}}^{\bar{\nu}_e p} L_{\bar{\nu}_e}, \end{aligned} \quad (27)$$

where d_z is the distance from neutrino production to Earth.

4.2 Neutrino effective potential

Neutrinos generated during this hypercritical phase and going through the star will oscillate in each zone depending on the neutrino effective potential.

4.2.1 Zone I

On the neutron star surface, the plasma is magnetized $1.0 \times 10^{12} < B < 5.0 \times 10^{12} \text{ G}$ (see Fig. 3) and thermalized at $1.3 < T < 7 \text{ MeV}$ (Fig. 3). In this regime, the neutrino effective potential is written as (Fraija 2014c, 2015a; Fraija & Bernal 2015)

$$\begin{aligned} V_{\text{eff},m} &= \frac{\sqrt{2} G_F m_e^3 B}{\pi^2 B_c} \left[\sum_{l=0}^{\infty} (-1)^l \sinh \alpha_l [F_m - G_m \cos \varphi] \right. \\ &\quad \left. - 4 \frac{m_e^2}{m_W^2} \frac{E_\nu}{m_e} \sum_{l=0}^{\infty} (-1)^l \cosh \alpha_l [J_m - H_m \cos \varphi] \right], \end{aligned} \quad (28)$$

where $B_c = 4.4 \times 10^{13} \text{ G}$, G_F is Fermi constant, m_W is the W-boson mass and the functions F_m , G_m , J_m , H_m are

$$\begin{aligned} F_m &= \left(1 + 2 \frac{E_\nu^2}{m_W^2} \right) K_1(\sigma_l) + 2 \sum_{n=1}^{\infty} \lambda_n \left(1 + \frac{E_\nu^2}{m_W^2} \right) K_1(\sigma_l \lambda_n) \\ G_m &= \left(1 - 2 \frac{E_\nu^2}{m_W^2} \right) K_1(\sigma_l) - 2 \sum_{n=1}^{\infty} \lambda_n \frac{E_\nu^2}{m_W^2} K_1(\sigma_l \lambda_n) \end{aligned}$$

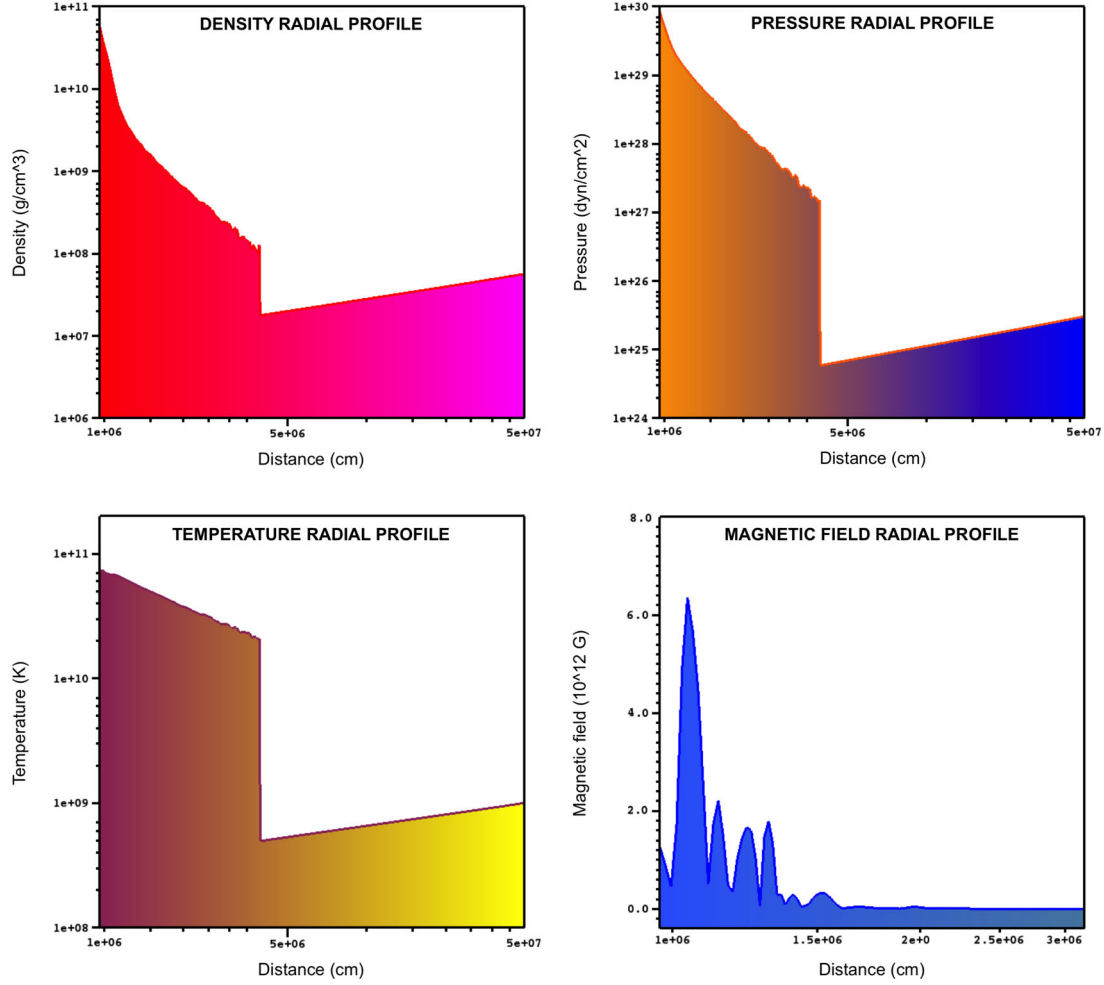


Figure 3. Radial profiles of density, pressure, temperature (on a logarithmic scale) and magnetic field (on a linear scale) for the Kes 79 hyperaccretion rate when a quasi-hydrostatic envelope has been established ($t = 150$ ms). The free-fall region, the quasi-hydrostatic envelope and the new crust are present.

$$J_m = \frac{3}{4}K_0(\sigma_l) + \frac{K_1(\sigma_l)}{\sigma_l} + \sum_{n=1}^{\infty} \lambda_n^2 \left[K_0(\sigma_l \lambda) + \frac{K_1(\sigma_l \lambda)}{\sigma_l \lambda} - \frac{K_0(\sigma_l \lambda)}{2\lambda_n^2} \right]$$

$$H_m = \frac{K_1(\sigma_l)}{\sigma_l} + \sum_{n=1}^{\infty} \lambda_n^2 \left[\frac{K_1(\sigma_l \lambda)}{\sigma_l \lambda} - \frac{K_0(\sigma_l \lambda)}{2\lambda_n^2} \right] \quad (29)$$

where $\lambda_n^2 = 1 + 2n B/B_c$, K_i is the modified Bessel function of integral order i , $\alpha_l = \beta\mu(l+1)$ and $\sigma_l = \beta m_e(l+1)$. It is important to clarify that as the magnetic field decreases the effective potential will depend less on the Landau levels.

4.2.2 Zones II, III and IV

In zones II, III and IV, neutrinos will undergo different effective potentials. It can be written as

$$V_{\text{eff}} = \sqrt{2}G_F N_A \rho(r) Y_e, \quad (30)$$

where Y_e is the number of electrons per nucleon and $\rho(r)$ is given in Table 1.

4.3 Neutrino oscillation

Measurements of the fluxes at solar, atmospheric and accelerator neutrinos have shown overwhelming evidence of neutrino oscillations and then neutrino masses and mixing. To make a full analysis, we are going to show the important quantities to involve in neutrino oscillations in vacuum and matter as well as the two- and three-mixing parameters. The two-mixing parameters are related as follows.

Solar experiments. A two-flavour neutrino oscillation analysis yielded $\delta m^2 = (5.6^{+1.9}_{-1.4}) \times 10^{-5} \text{ eV}^2$ and $\tan^2 \theta = 0.427^{+0.033}_{-0.029}$ (Aharmim et al. 2013).

Atmospheric experiments. Under a two-flavour disappearance model with separate mixing parameters between neutrinos and antineutrinos, the following parameters for the SK-I + II + III data $\delta m^2 = (2.1^{+0.9}_{-0.4}) \times 10^{-3} \text{ eV}^2$ and $\sin^2 2\theta = 1.0^{+0.00}_{-0.07}$ were found (Abe et al. 2011).

Accelerator experiments. Church et al. (2002) found two well-defined regions of oscillation parameters with either $\delta m^2 \approx 7 \text{ eV}^2$ or $\delta m^2 < 1 \text{ eV}^2$ compatible with both lead astronomical neutrino detector (LAND) and Karlsruhe-Rutherford Medium Energy Neutrino experiments, for the complementary confidence and the angle mixing is $\sin^2 \theta = 0.0049$. In addition, MiniBooNE found evidence of oscillations in the $0.1\text{--}1.0 \text{ eV}^2$, which are consistent with LAND results (Athanasopoulos et al. 1996, 1998).

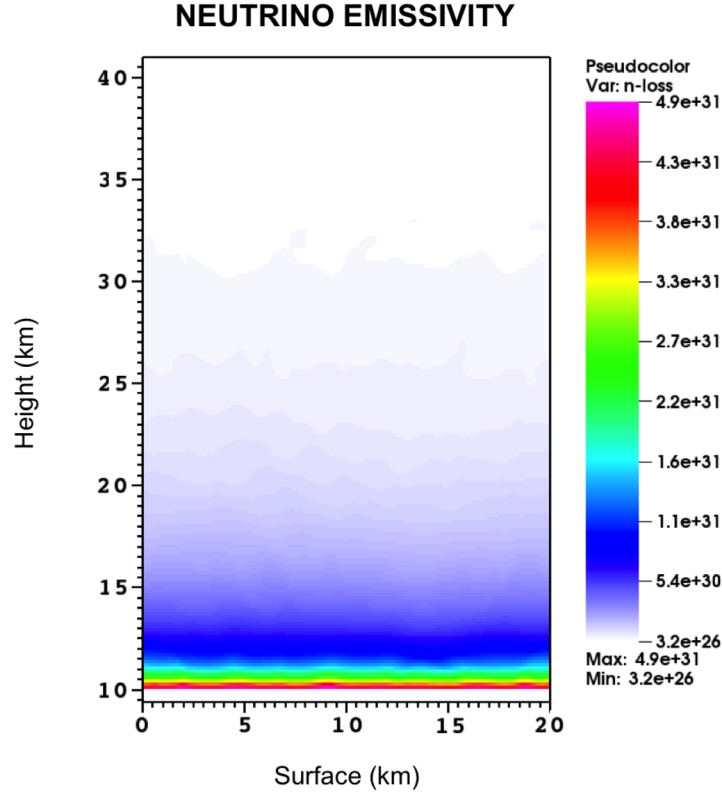


Figure 4. Colour map, in linear scale, of the neutrino emissivity when the quasi-stationary state is reached ($t = 150$) ms. Note the strong emissivity concentrated very close to the stellar surface.

The combining solar, atmospheric and accelerator parameters are related in three-mixing parameters as follows (Wendell et al. 2010; Aharmim et al. 2013):

$$\begin{aligned} \text{for } \sin^2_{13} < 0.053 : \delta m^2_{21} &= (7.41^{+0.21}_{-0.19}) \times 10^{-5} \text{ eV}^2 \\ &\text{and } \tan^2 \theta_{12} = 0.446^{+0.030}_{-0.029} \\ \text{for } \sin^2_{13} < 0.04 : \delta m^2_{23} &= (2.1^{+0.5}_{-0.2}) \times 10^{-3} \text{ eV}^2 \\ &\text{and } \sin^2 \theta_{23} = 0.50^{+0.083}_{-0.093}. \end{aligned} \quad (31)$$

4.3.1 In vacuum

Neutrino oscillation in vacuum would arise if neutrinos were massive and mixed. For massive neutrinos, the weak eigenstates ν_α are linear combinations of mass eigenstates $|\nu_\alpha\rangle = \sum_{i=1}^n U_{\alpha i}^* |\nu_i\rangle$. After travelling a distance $L \simeq ct$, a neutrino produced with flavour α evolves to $|\nu_\alpha(t)\rangle = \sum_{i=1}^n U_{\alpha i}^* |\nu_i(t)\rangle$. Then, the transition probability from a flavour state α to a flavour state β can be written as $P_{\nu_\alpha \rightarrow \nu_\beta} = \delta_{\alpha\beta} - 4 \sum_{j>i} U_{\alpha i} U_{\beta i} U_{\alpha j}^* U_{\beta j}^* \sin^2[\delta m^2_{ij} L / (4 E_\nu)]$ with L being the distance travelled by the neutrino in reaching Earth (detector). Using the set of parameters given in equation (31) and averaging the sin term in the probability to ~ 0.5 for larger distances L (longer than the Solar system; Learned & Pakvasa 1995), the probability matrix for a neutrino flavour vector of $(\nu_e, \nu_\mu, \nu_\tau)_{\text{source}}$ changing to a flavour vector $(\nu_e, \nu_\mu, \nu_\tau)_{\text{Earth}}$ is given as

$$\begin{pmatrix} \nu_e \\ \nu_\mu \\ \nu_\tau \end{pmatrix}_E = \begin{pmatrix} 0.534 & 0.265 & 0.200 \\ 0.265 & 0.366 & 0.368 \\ 0.200 & 0.368 & 0.431 \end{pmatrix} \times \begin{pmatrix} \nu_e \\ \nu_\mu \\ \nu_\tau \end{pmatrix}_S \quad (32)$$

where E and S are Earth and source, respectively.

4.3.2 In matter

4.3.2.1 Two-neutrino mixing. The evolution equation for the propagation of neutrinos in the above medium is given by (Fraija 2016)

$$i \begin{pmatrix} \dot{\nu}_e \\ \dot{\nu}_\mu \end{pmatrix} = \begin{pmatrix} V_{\text{eff},s/m} - \Delta \cos 2\theta & \frac{\Delta}{2} \sin 2\theta \\ \frac{\Delta}{2} \sin 2\theta & 0 \end{pmatrix} \begin{pmatrix} \nu_e \\ \nu_\mu \end{pmatrix}, \quad (33)$$

where $\Delta = \delta m^2 / 2E_\nu$, $V_{\text{eff},s/m}$ is the effective potential given by equation (28), E_ν is the neutrino energy and θ is the neutrino mixing angle. Here we have considered the neutrino oscillation process $\nu_e \leftrightarrow \nu_\mu, \tau$. The transition probability in matter is $P_{\nu_e \rightarrow \nu_\mu(\nu_\tau)}(t) = \frac{\Delta^2 \sin^2 2\theta}{\omega^2} \sin^2\left(\frac{\omega t}{2}\right)$ with $\omega = \sqrt{(V_{\text{eff}} - \Delta \cos 2\theta)^2 + \Delta^2 \sin^2 2\theta}$. This probability has an oscillatory behaviour, with oscillation length given by

$$L_{\text{osc}} = \frac{L_\nu}{\sqrt{\cos^2 2\theta \left(1 - \frac{V_{\text{eff}}}{\Delta \cos 2\theta}\right)^2 + \sin^2 2\theta}}, \quad (34)$$

where $L_\nu = 2\pi/\Delta$ is the vacuum oscillation length. Satisfying the resonance condition

$$V_{\text{eff}} - \frac{\delta m^2}{2E_\nu} \cos 2\theta = 0, \quad (35)$$

the resonance length can be written as $L_{\text{res}} = \frac{L_\nu}{\sin 2\theta}$.

4.3.2.2 Three-neutrino mixing. The neutrino dynamics is determined by the evolution equation in a three-flavour framework which can be written as

$$i \frac{d\mathbf{v}}{dt} = H \mathbf{v}, \quad (36)$$

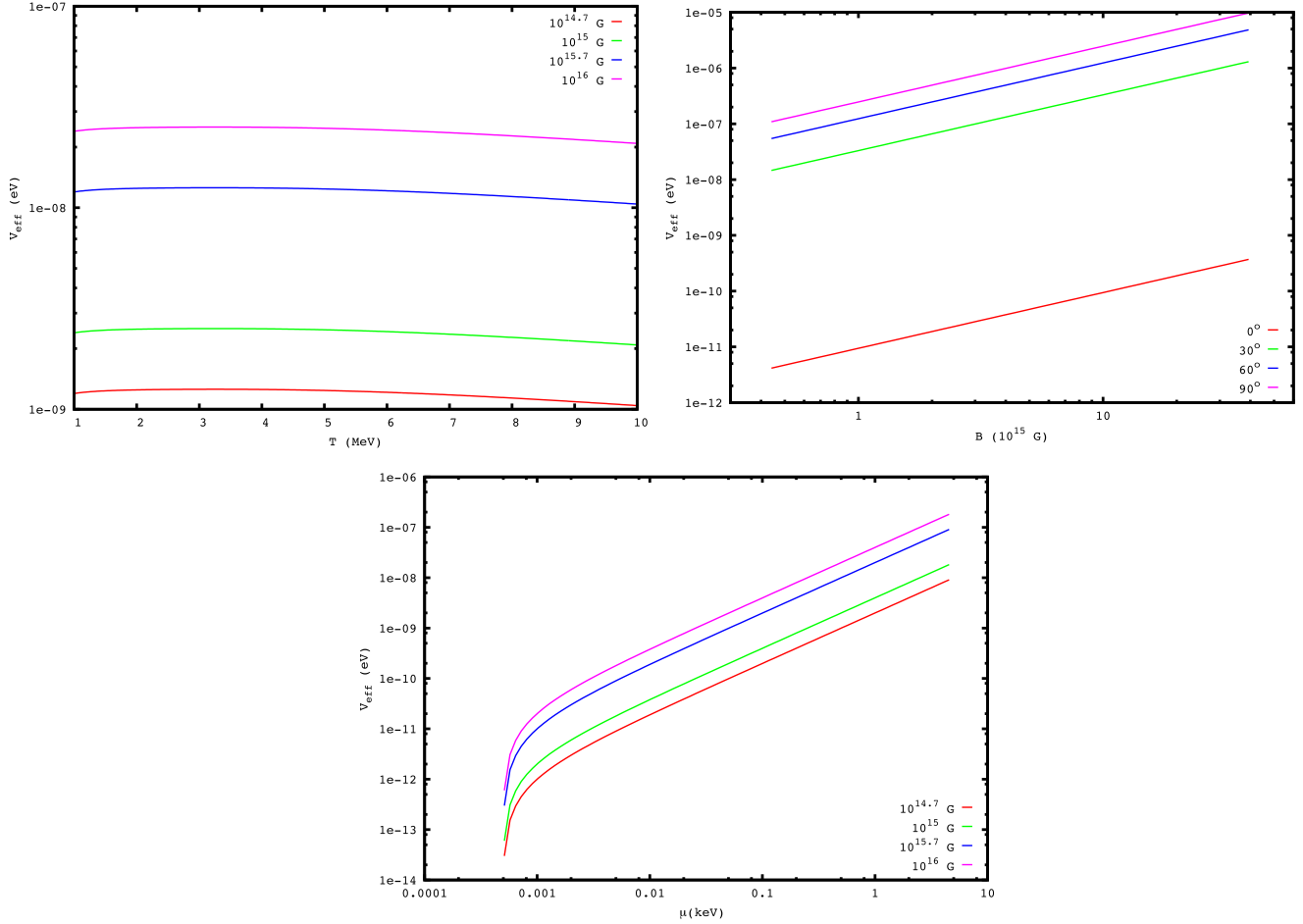


Figure 5. Neutrino effective potential in the moderate magnetic field regime as a function of temperature (top left), magnetic field (top right) and chemical potential (bottom).

and the state vector in the flavour basis is defined as

$$\mathbf{v} \equiv (v_e, v_\mu, v_\tau)^T. \quad (37)$$

The effective Hamiltonian is (Fraija 2014d)

$$H = U \cdot H_0^d \cdot U^\dagger + \text{diag}(V_{\text{eff}}, 0, 0), \quad (38)$$

with

$$H_0^d = \frac{1}{2E_\nu} \text{diag}(-\delta m_{21}^2, 0, \delta m_{32}^2). \quad (39)$$

Here U is the three-neutrino mixing matrix given by Gonzalez-Garcia & Nir (2003), Akhmedov et al. (2004), Gonzalez-Garcia & Maltoni (2008) and Gonzalez-Garcia (2011). The oscillation length of the transition probability is given by

$$l_{\text{osc}} = \frac{l_\nu}{\sqrt{\cos^2 2\theta_{13} \left(1 - \frac{2E_\nu V_e}{\delta m_{32}^2 \cos 2\theta_{13}}\right)^2 + \sin^2 2\theta_{13}}}, \quad (40)$$

where $l_\nu = 4\pi E_\nu / \delta m_{32}^2$ is the vacuum oscillation length. The resonance condition and resonance length are

$$V_{\text{eff}} - 5 \times 10^{-7} \frac{\delta m_{32}^2 \text{eV}}{E_{\nu, \text{MeV}}} \cos 2\theta_{13} = 0 \quad (41)$$

and $l_{\text{res}} = \frac{l_\nu}{\sin 2\theta_{13}}$. Considering the adiabatic condition at the resonance, it is expressed as (Fraija 2015b)

$$\kappa_{\text{res}} \equiv \frac{2}{\pi} \left(\frac{\delta m_{32}^2 \sin 2\theta_{13}}{2E_\nu} \right)^2 \left(\frac{dV_{\text{eff}}}{dr} \right)^{-1} \geq 1. \quad (42)$$

5 CONCLUSIONS

In the present work, we have studied the dynamics of hyperaccretion (with neutrino emission) on to a newly born neutron star as is the case of Kes 79 scenario. To do this, we have performed numerical 2D MHD simulations using the AMR FLASH method. The code allows us to capture the rich morphology and the main characteristics of the fundamental physical processes in detail. We included a custom routine in the code that takes into account several neutrino-cooling processes, which are active depending on strict criteria of temperature and density of the model in the computational domain. With this, we found that for the estimated hyperaccretion rate for the Kes 79 scenario, the bulk of magnetic field is submerged efficiently into the new crust formed by the accreted matter during this regime. Additionally, we found that the code reproduces the radial profile of the main thermodynamical parameters of the hypercritical regime, including the accretion shock radius, which is in good agreement with the value analytically estimated. It is noteworthy that a (completely relaxed) steady state could not be reached, within the parameters

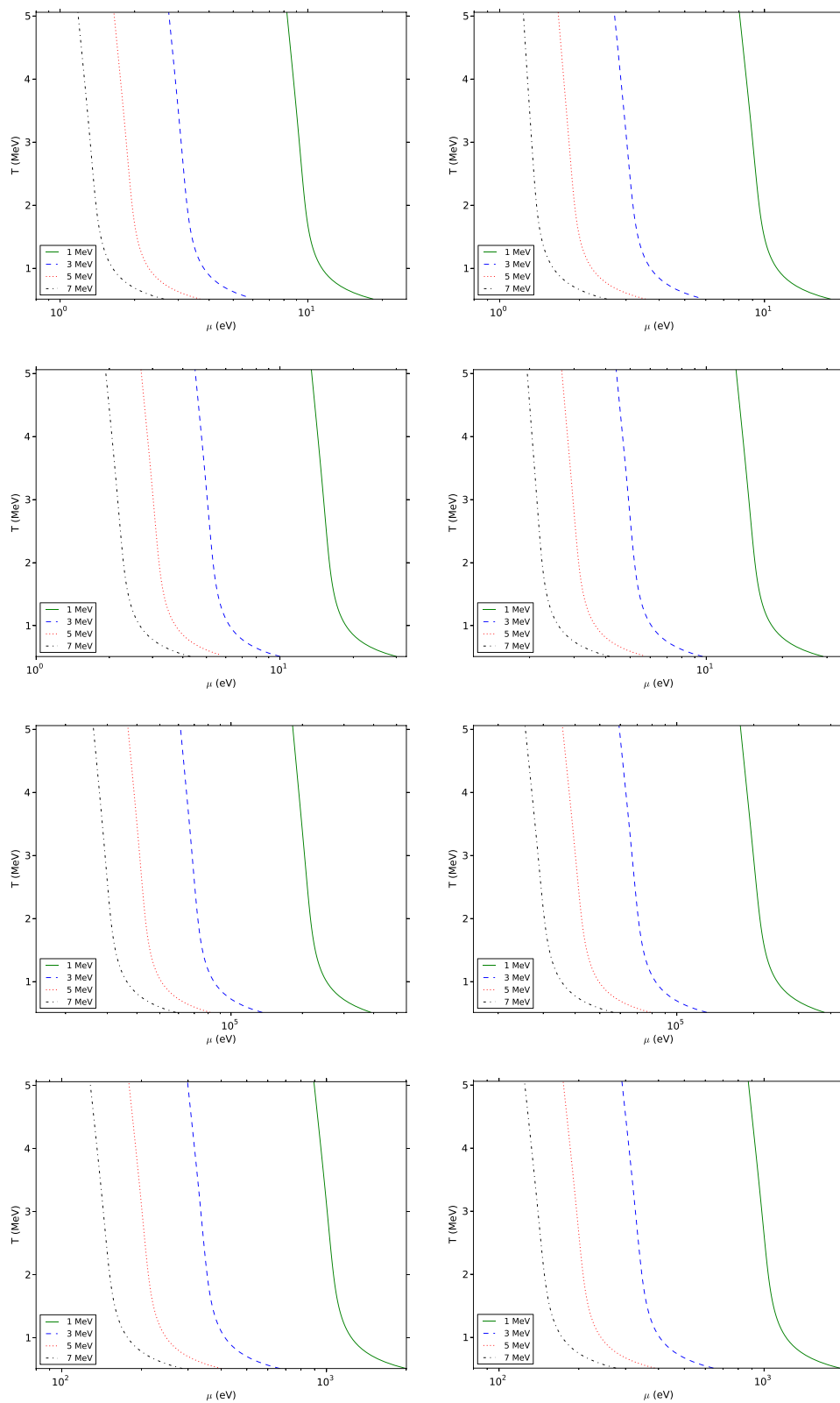


Figure 6. Contour plots of temperature (T) and chemical potential (μ) as a function of neutrino energy for which the resonance condition is satisfied. We have applied the neutrino effective potential at the moderate field limit, two values of angles $\phi = 0^\circ$ (left column) and $\phi = 90^\circ$ (right column). We have used the best-fitting values of neutrino mixing. From top to bottom: solar, atmospheric, accelerator and three flavours.

Table 2. The neutrino flavour ratio in each region of the hypercritical phase for $E_\nu = 1, 3, 5$ and 7 MeV.

E_ν	On the NS surface	Accretion material	Free-fall zone	Outer layers	On Earth
1	1.2:0.9:0.9	1.186:0.907: 0.907	1.152:0.924:0.924	1.120:0.940:0.940	1.036:0.988:0.976
3	1.2:0.9:0.9	1.161:0.919:0.919	1.130:0.935:0.935	1.132:0.934: 0.934	1.039:0.987:0.974
5	1.2:0.9:0.9	1.159:0.921:0.921	1.127:0.937:0.937	1.123:0.938:0.938	1.037:0.987:0.975
7	1.2:0.9:0.9	1.172: 0.914:0.914	1.142:0.929:0.929	1.135:0.933:0.933	1.041:0.987:0.973

of the simulation, due to various factors: periodicity of the lateral boundaries, effects of buoyancy and magnetic stresses near the stellar surface, among others. Also, although most of the magnetic field is confined/submerged in the stellar crust, residual weak magnetic field is present within the quasi-hydrostatic envelope but that does not influence the dynamics of the system.

Once the hypercritical phase ends, the story for the magnetic field continues. Muslimov & Page (1995) found that after hyperaccretion stopped, the bulk of the submerged magnetic field could diffuse back to the surface by ohmic processes and depending on the amount of accreted matter, the submergence could be so deep that the neutron star may appear and remain unmagnetized for centuries. It is possible that, in addition to the ohmic diffusion of the bulk of the magnetic field, some portion of the confined magnetic field may be pushed into the neutron star by the hyperaccretion, and it may be crystallized in the mantle. The presence of a crystal lattice of atomic nuclei in the crust is mandatory for modelling of the subsequent radio-pulsar glitches (see Geppert et al. 1999 and references therein). Presence of solid crust enables excitation of toroidal modes of oscillations. The toroidal modes in a completely fluid star have all zero frequency, but the presence of a solid crust gives them non-zero frequencies in the range of kHz. On the other hand, requiring the value of distance $d_z = 7.1$ kpc (Case & Bhattacharya 1998), neutrino Luminosity $L_{\bar{\nu}_e} = (8.4 \pm 0.4) \times 10^{48}$ erg s $^{-1}$ (this work, Fig. 4), effective volume of HK, $V \simeq 0.56 \times 10^{12}$ cm 3 (Hyper-Kamiokande Working Group et al. 2014) and the average neutrino energy ($E_{\bar{\nu}_e}$) $\simeq 7$ MeV, from equation (27) we obtain that the number of events that could have been expected from the hypercritical phase on HK is 733 ± 364 . In addition, we compute the number of initial neutrino burst expected during the neutron star formation. Taking into account a temperature $T \approx 4 \pm 1$ MeV (Giunti & Kim 2007), a duration of the neutrino pulse in the hypercritical phase $t \simeq 10^3$ s, the average neutrino energy ($E_{\bar{\nu}_e}$) $\simeq 13.5 \pm 3.2$ MeV (Giunti & Kim 2007) and a total fluence equivalent of Kes 79 $\Phi \approx (1.25 \pm 0.52) \times 10^{11}$ $\bar{\nu}_e$ cm $^{-2}$ (Bahcall 1989; Mohapatra & Pal 2004), then the total number of neutrinos emitted from Kes 79 would be $N_{\text{tot}} = 6 \Phi 4\pi d_z^2 \approx (8.97 \pm 3.58) \times 10^{57}$. Similarly, we can compute the total radiated luminosity corresponding to the binding energy of the neutron star $L_\nu \approx \frac{N_{\text{tot}}}{t} \times \langle E_{\bar{\nu}_e} \rangle \approx (2.16 \pm 0.87) \times 10^{52}$ erg s $^{-1}$. Regarding the effective volume $V \simeq 0.56 \times 10^{12}$ cm 3 (Hyper-Kamiokande Working Group et al. 2014), from equation (27) we get $N_{\text{ev}} \simeq 1129 \pm 475$ events expected during the neutron star formation in a neutrino detector as HK experiment. Comparing the number of neutrinos expected during the neutron star formation and the hyperaccretion phase, we obtain 1.5 events.

Neutrinos generated at the hypercritical accretion phase will oscillate in their ways due to electron density in zones I, II, III and IV, and after in vacuum into Earth. In zone I, the thermal plasma is endowed with a magnetic field $\sim (1-6) \times 10^{12}$ G and thermalized $\sim (1-8)$ MeV. Taking into account the neutrino effective potential given in zone I, we plot the neutrino effective potential as a function of magnetic field, angle, temperature and chemical potential. From Fig. 5 can be observed the positivity of the effective potential

($V_{\text{eff}} > 0$); therefore, neutrinos can oscillate resonantly. Taking into account the two- and three-neutrino mixing parameters, we analyse the resonance condition, as shown in Fig. 6. Recently, Fraija et al. (2014) showed that neutrinos can oscillate resonantly due to the density profiles of the collapsing material surrounding the progenitor. In zones II, III and IV, the author showed that neutrinos can oscillate resonantly and computed the survival and conversion probabilities for the active-active ($\nu_e, \mu, \tau \leftrightarrow \nu_e, \mu, \tau$) neutrino oscillations in each region. Taking into account the oscillation probabilities in each region and in the vacuum (on its path to Earth), we calculate the flavour ratio expected on Earth for neutrino energies of $E_\nu = 1, 1, 3, 5$ and 7 MeV, as shown in Table 2. In this table, we can see a small deviation from the standard ratio flavour 1:1:1. In this calculation, we take into account that for neutrino-cooling processes (electron-positron annihilation, inverse beta decay, nucleonic bremsstrahlung and plasmons), only inverse beta decay is the one producing electron neutrino. It is worth noting that our calculations of resonant oscillations were performed for neutrinos instead of antineutrinos, due to the positivity of the neutrino effective potential.

As a final remark, we can say that the present numerical studies of these phenomena are necessary and very important, and its results can give us a glimpse of the complex dynamics around the newly born neutron stars, moments after the core-collapse SN explosion. Although we use the Kes 79 as a particular case of the hidden magnetic field scenario, this method can be applied to the various CCOs scenarios. Nevertheless, the eventual growing of the bulk magnetic field post-hyperaccretion, the possible magnetic field amplification by turbulent dynamo and the magnetic field crystallization processes inside neutron star require more detailed studies that are outside the scope of this paper.

ACKNOWLEDGEMENTS

We thank the anonymous referee for a critical reading of the paper and valuable suggestions that helped improve the quality and clarity of this work. We also thank to Dany Page, John Beacom and W. H. Lee for useful discussions. CB acknowledges to CAPES–Brazil by the postdoctoral fellowship received through the Science Without Borders programme. This work was supported by the projects IG100414 and Conacyt 101958. The software used in this work was in part developed by the DOE NNSA-ASC OASCR FLASH Center at the University of Chicago.

REFERENCES

- Abe K. et al., 2011, Phys. Rev. Lett., 107, 241801
- Aharmim B. et al., 2013, Phys. Rev. C, 88, 025501
- Akhmedov E. K., Johansson R., Lindner M., Ohlsson T., Schwetz T., 2004, J. High Energy Phys., 4, 78
- Athanassopoulos C. et al., 1996, Phys. Rev. Lett., 77, 3082
- Athanassopoulos C. et al., 1998, Phys. Rev. Lett., 81, 1774
- Bahcall J. N., 1989, Neutrino Astrophysics. Cambridge Univ. Press, Cambridge

- Bernal C. G., Lee W. H., Page D., 2010, *Rev. Mex. Astron. Astrofis.*, 46, 309
- Bernal C. G., Page D., Lee W. H., 2013, *ApJ*, 770, 106
- Bilenky S., Hošek J., 1982, *Phys. Rep.*, 90, 73
- Bogdanov S., 2014, *ApJ*, 790, 94
- Case G. L., Bhattacharya D., 1998, *ApJ*, 504, 761
- Chakrabarty D., Pivovarov M. J., Hernquist L. E., Heyl J. S., Narayan R., 2001, *ApJ*, 548, 800
- Chevalier R. A., 1989, *ApJ*, 346, 847
- Chevalier R. A., 2005, *ApJ*, 619, 839
- Chevalier R. A., Soker N., 1989, *ApJ*, 341, 867
- Church E. D., Eitel K., Mills G. B., Steidl M., 2002, *Phys. Rev. D*, 66, 013001
- Dicus D. A., 1972, *Phys. Rev. D*, 6, 941
- Fraija N., 2014a, *ApJ*, 783, 44
- Fraija N., 2014b, *MNRAS*, 441, 1209
- Fraija N., 2014c, *ApJ*, 787, 140
- Fraija N., 2014d, *MNRAS*, 437, 2187
- Fraija N., 2015a, *Astropart. Phys.*, 71, 1
- Fraija N., 2015b, *MNRAS*, 450, 2784
- Fraija N., 2016, *High Energy Astrophys.*, 9, 25
- Fraija N., Araya M., 2016, *ApJ*, 826, 31
- Fraija N., Bernal C. G., 2015, *MNRAS*, 451, 455
- Fraija N., Bernal C. G., Hidalgo-Gaméz A. M., 2014, *MNRAS*, 442, 239
- Fraija N., Marinelli A., 2015, *Astropart. Phys.*, 70, 54
- Fryxell B. et al., 2000, *ApJS*, 131, 273
- Geppert U., Page D., Zannias T., 1999, *A&A*, 345, 847
- Giunti C., Kim C. W., 2007, *Fundamentals of Neutrino Physics and Astrophysics*. Oxford Univ. Press, Oxford, UK
- Gonzalez-Garcia M. C., 2011, *Phys. Part. Nucl.*, 42, 577
- Gonzalez-Garcia M. C., Maltoni M., 2008, *Phys. Rep.*, 460, 1
- Gonzalez-Garcia M. C., Nir Y., 2003, *Rev. Mod. Phys.*, 75, 345
- Gotthelf E. V., Halpern J. P., Seward F. D., 2005, *ApJ*, 627, 390
- Ho W. C. G., 2011, *MNRAS*, 414, 2567
- Hyper-Kamiokande Working Group et al., 2014, preprint ([arXiv:e-prints](https://arxiv.org/abs/1405.0001))
- Itoh N., Hayashi H., Nishikawa A., Kohyama Y., 1996, *ApJS*, 102, 411
- Kaspi V. M., 2010, *Proc. Natl. Acad. Sci.*, 107, 7147
- Kesteven M. J. L., 1968, *Aust. J. Phys.*, 21, 739
- Learned J. G., Pakvasa S., 1995, *Astropart. Phys.*, 3, 267
- Mohapatra R. N., Pal P. B., 2004, *Massive Neutrinos in Physics and Astrophysics*. World Scientific, New Jersey, NJ
- Muslimov A., Page D., 1995, *ApJ*, 440, L77
- Pavlov G. G., Sanwal D., Teter M. A., 2004, in Camilo F., Gaensler B. M., eds, *Proc. IAU Symp. 218, Young Neutron Stars and Their Environments*. Astron. Soc. Pac., San Francisco, p. 239
- Popov S. B., Kaurov A. A., Kaminker A. D., 2015, *PASA*, 32, 18
- Powell K. G., Roe P. L., Linde T. J., Gombosi T. I., De Zeeuw D. L., 1999, *J. Comput. Phys.*, 154, 284
- Rrapaj E., Holt J. W., Bartl A., Reddy S., Schwenk A., 2015, *Phys. Rev. C*, 91, 035806
- Scholberg K., 2012, *Annu. Rev. Nucl. Part. Sci.*, 62, 81
- Seward F. D., Slane P. O., Smith R. K., Sun M., 2003, *ApJ*, 584, 414
- Shabaltas N., Lai D., 2012, *ApJ*, 748, 148
- Timmes F. X., Swesty F. D., 2000, *ApJS*, 126, 501
- Torres-Forné A., Cerdá-Durán P., Pons J. A., Font J. A., 2016, *MNRAS*, 456, 3813
- Viganò D., Pons J. A., 2012, *MNRAS*, 425, 2487
- Wendell R. et al., 2010, *Phys. Rev. D*, 81, 092004
- Wolfenstein L., 1978, *Phys. Rev. D*, 17, 2369
- Woosley S. E., Langer N., Weaver T. A., 1993, *ApJ*, 411, 823

This paper has been typeset from a $\text{\TeX}/\text{\LaTeX}$ file prepared by the author.